Novella Rosa, R.; Gómez-Soriano, J.; Barbery-Avila, II.; Cédric Libert (2022). Numerical analysis of the passive pre-chamber ignition concept for light duty applications. Applied Thermal Engineering. 213:1-16. https://doi.org/10.1016/j.applthermaleng.2022.118610

Numerical analysis of the passive pre-chamber ignition concept for light duty applications

R. Novella[a], J. Gomez-Soriano[a,*], I. Barbery[a], C. Libert[b]

[a]*CMT – Motores Térmicos, Universitat Politècnica de València, Camino de Vera, 46022 Valencia, Spain*
[b]*DEA-IRP Groupe Renault, 1 avenue du Golf. 78084, Guyancourt, France*

Abstract

The use of advanced ignition concepts and enhanced combustion strategies is being widely studied for modern engine applications. In this framework, the passive pre-chamber ignition system is gaining popularity for its mechanical simplicity. However, in order to implement this ignition system in passenger car vehicles, the concept must be able to operate in the whole engine map. Numerous experimental investigations in the literature have found that the concept operates suitably at high load/speed conditions but has several problems operating at low engine load/speeds. However, not many investigation conducted to date have focused on comparing and understanding the underlying physics of this ignition strategy in different engine load/speed conditions. Therefore, in this investigation, a numerical study is carried out using a state of the art 3D-CFD model, to analyze the performance of the passive pre-chamber ignition system in three relevant operating conditions of the engine map. A novel methodology is developed to analyze the fundamentals of the passive pre-chamber concept in terms of internal flow field characteristics, combustion and energy conversion. The model is validated with experiments performed previously by the authors. In particular, the low load/speed operating point, representative of idle conditions, was deeply analyzed to asses the issues reported in the literature. Results have shown that the inherent deterioration of the flow field properties inside the pre-chamber as the engine load/speed decreases, compromises the operation at low load/speed conditions. The energy conversion in the pre-chamber is also worsened when operating at lower load/speeds, hindering the generation of suitable jets for igniting the main chamber charge. Moreover, the position of the pre-chamber in the cylinder head has a significant impact on the energy distribution in the main chamber. The results also revealed that a higher amount of non-reacting/cold flow is ejected from the pre-chamber as the spark is pushed from MBT conditions towards the top dead center (TDC), and the gap between the triggering of the spark and the onset of main chamber combustion increases. The findings of this article have allowed to close the knowledge gap between the physical characteristics of the passive pre-chamber concept and the experimental trends found in other researches on this topic.

Keywords: *Spark-Ignition engines, Computational Fluid Dynamics, Passive Pre-chamber ignition, Combustion process analysis, Energy conversion*

1. Introduction

Modern society will face challenging times in the upcoming years. Most means of energy production are still fossil fuel dependent, and this is generating a growing concern about their impact on global warming and pollution. Over 25% of the energy produced worldwide is consumed by transportation [1]. This sector is also responsible for a high percentage of carbon dioxide (CO_2) emissions and hazardous pollutants like carbon monoxide (CO) and nitrogen oxides (NO_x) [2]. In particular, road transportation accounts for most of these emissions [3]. For this reason, a number of global treaties and several governments are implementing restrictive policies to reduce the environmental footprint of transportation [4, 5]. Engine manufacturers are being forced to develop new power trains able to comply with these restrictions, without excessively compromising the performance of the vehicle. The combination of different technological bricks for improving the thermal efficiency of the engine while reducing pollutant emissions, is required to achieve this goal.

Nowadays, most of passenger car vehicles have shifted from Diesel compression ignition (CI) engines to gasoline fueled spark ignition (SI) engines. This trend is mainly related to environmental aspects, given that the after-treatment systems required in CI engines to maintain tailpipe emissions below the European standards are more expensive than those required by SI engines [6, 7]. Nevertheless, SI engines have considerable disadvantages in terms of thermal efficiency due to knocking combustion limitations [8, 9]. This phenomenon prevents the use of high compression ratios, since it could compromise the mechanical integrity of the engine. Additionally, these engines need to be operated at stoichiometric air-to-fuel ratios ($\lambda \sim 1$) to be compatible with the Three-Way Catalyst (TWC) for controlling NO_x emissions [10]. These

*Corresponding author.
Tel.: +34 96 387 98 13, fax: +34 96 387 76 59
email: jogoso1@mot.upv.es

requirements have motivated many researchers to evaluate modern strategies in the search of higher thermal efficiencies.

A promising alternative for future SI engines is the use of enhanced combustion strategies and advanced ignition systems. In this framework, the pre-chamber ignition concept [11, 12], or its commercial name "Turbulent Jet Ignition" (TJI), is gaining interest as a solution for increasing thermal efficiency. This strategy places the standard spark plug inside a confined volume called a "pre-chamber". Multiple holes are manufactured in the bottom part of the pre-chamber, connecting this region with the main combustion chamber [13, 14]. These holes are typically cylinders, with lengths between 1 mm and 2 mm for light duty engine applications. The pre-chamber usually constitutes between 2% and 5% of the combustion chamber volume at the Top Dead Center (TDC) [15, 16].

In this strategy, the combustion process starts inside the pre-chamber. As the flame propagates in this region, the pressure rises, forcing the gas to move towards the bottom of the pre-chamber, where the holes are located. Then, as a result of the stretching through the small holes, a series of jets penetrate into the main chamber, igniting the charge with a larger flame surface at multiple locations. The jets distribute burned products as they sweep the main chamber volume, generating uniform and dispersed ignition. Moreover, the turbulence generated by the shear stress of the flow through the holes increases the flame propagation speed [17]. Consequently, higher combustion rates are achieved, enabling the use of higher compression ratios as the charge is completely burned before exceeding the auto-ignition delay time.

The pre-chamber ignition concept has been successfully implemented in high-power stationary power plants [18]. In these applications, the system is usually implemented by an active approach, with an auxiliary fuel supplier inside the pre-chamber. Therefore, the air-to-fuel ratio in this region can be controlled independently from the main chamber charge. In addition, the engine is able to operate at high dilution rates as a fast pre-chamber combustion is guaranteed, and the ejected jets are strong enough to burn extremely lean environments [19, 20, 21]. Nevertheless, the extra-cost of manufacturing and installing the auxiliary fuel injector is very high, making this approach unpractical for passenger car applications.

A different approach for implementing this ignition strategy is through a passive system. In this case, the pre-chamber does not have an auxiliary fuel injector, thus its air-to-fuel ratio is not directly controlled [22, 23]. In Port Fuel Injection (PFI) engines, the main chamber and the pre-chamber charge share basically the same mixture composition. Therefore, the passive pre-chamber system has inherent disadvantages compared to the active system, given that the pre-chamber jets are not suitable in all conditions. Thus, understanding the underlying physics of the concept in the whole engine map becomes crucial for considering this technology as a mid-term solution for improving the performance of automotive vehicles.

Several studies in the literature have evaluated the use of passive pre-chambers in SI engines through experimental test campaigns. Benajes et al. [24] compared the passive pre-chamber ignition concept with a conventional spark ignition system in a turbocharged gasoline fueled SI engine with a geometric compression ratio of 13.4:1. In this investigation, relevant improvements were found in terms of engine indicated efficiency (around 3% of efficiency gain) when operating with the passive pre-chamber concept under knock limited conditions (i.e high engine load/speed conditions), given that the faster burning rates achieved with this ignition system allowed to improve the combustion phasing in the aforementioned conditions. In another study, Lopez et al. [25] evaluated the passive pre-chamber concept against the conventional spark ignition system in a similar engine fueled with Compressed Natural Gas (CNG). This investigation showed that at low engine load/speed conditions the efficiency levels achieved with passive pre-chamber operation were lower than the ones achieved with the conventional spark plug. This trend was confirmed by Novella et al. [26] in a study that evaluated the pre-chamber concept in a high compression ratio (15.4:1) SI engine fueled with CNG and using a Miller Cycle camshaft.

All these investigations, despite using different combinations of fuels and engine architectures, showed a common issue regarding the low performance of the passive pre-chamber system at low engine load/speeds. A well-documented and interesting trend found in the literature [27] is the inability to delay the combustion process towards the expansion stroke when operating at low load/speed conditions with the passive pre-chamber concept. In these conditions, a sharp increase in the cycle-to-cycle variations (CCV) is observed as the spark timing is pushed towards TDC, destabilizing the engine operation and compromising the efficiency levels. Furthermore, this phenomenon presents a major hurdle for implementing the technology in passenger car engines.

More and more modern investigations are implementing High Performance Computing (HPC) and state of the art numerical tools in their research methodologies. Particularly in engine research, Computational Fluid Dynamics (CFD) has allowed to study the combustion process of pre-chamber ignited engines in detail. Hu et al. [28] has used CFD to study the passive pre-chamber concept in an aviation kerosen engine, Posch et al. [29] has applied CFD combined with an artificial neural network (ANN) to research the pre-chamber system implemented in a heavy duty gas engine, and Benajes et al. [30, 31] has performed dedicated CFD studies of the passive pre-chamber ignition concept in light duty engines operating at extremely diluted conditions.

Nevertheless, Most of these numerical investigations focus on a single operating condition (load/speed) within the engine map, whereas almost no research conducted to date has simultaneously compared the pre-chamber ignition concept at very different operating points in terms of engine load and speed by advanced numerical simulations. Thus, understanding key aspects of the pre-chamber combustion pro-

cess in conditions where the concept performs suitably (high load/speeds) and conditions where the system presents problems (low load/speeds) can help to solve the issues found in the current literature.

Furthermore, in this article a numerical study is carried out using a state of the art CFD model of a light duty engine, well validated with experimental results, to investigate the underlying physics of the passive pre-chamber concept in key operating conditions. A novel methodology was developed to analyze the most relevant aspects of the concept in terms of energy conversion and combustion evolution in both the pre-chamber and main chamber. Particularly, the low load/speed operating point was deeply studied by performing a spark timing sweep with the numerical model. The main objective of the research is to improve knowledge of the passive pre-chamber ignition system in a wide range of the engine map, in order to shed some light on the issues encountered at low load/speed conditions.

2. Tools and methodology

The experimental setup, the numerical tools, the model validation and the methodology are described in this section.

2.1. Experimental facilities

A research version of a single-cylinder 4-stroke turbocharged SI engine fueled with RON95 gasoline was used for the experimental campaign. Among its features, the combination of a high compression ratio (13.4:1) with low cylinder displacement (404 cm^3) made this powertrain a representative sample of near future passenger car engines. A Port Fuel Injection (PFI) system was installed in the intake manifold, far enough from the cylinder head to guarantee a homogeneous air-fuel mixture to enter the cylinder. Standard double-overhead camshafts (DOHC) were considered for the valve distribution system. Regarding the ignition, a standard M12 screw was installed over the cylinder head, allowing to easily switch between the conventional spark plug and passive pre-chamber spark plugs. A summary of the most relevant features of the engine is shown in Table 1.

Table 1: *Main specifications of the engine.*

Engine	**4-stroke SI**
Number of cylinders [-]	1
Displacement [cm^3]	404
Bore – Stroke [mm]	80.0 – 80.5
Compression ratio (geometric) [-]	13.4:1
Valvetrain [-]	DOHC
Number of valves/cylinder [-]	2 intake and 2 exhaust
Fuel injection system [-]	PFI (p_{max} = 6 bar)

A schematic representation of the test bench where the engine was assembled is shown in Fig. 1. The bench counted with several equipment, hardware and sensors to measure and control relevant engine parameters, such as the temperature of the fuel, oil and coolant, instantaneous pressure signals in the intake, exhaust and cylinder with a resolution of 0.2 crankangle degrees (CAD), fuel consumption, in-cylinder air-to-fuel ratio and pollutant emissions. The full details of the test cell can be found in previous investigations by the authors [24, 32].

The experiments considered for this study were carried out at the operating conditions shown in Table 2. These three points are key conditions that gather a complete diagonal of the engine map, being appropriate for a full characterization of the concept. The low load/speed operating point (1350 rpm, 2.8 bar IMEP) is representative of idle conditions (for example when the car stops at a traffic light). The medium load/speed operating condition (2000 rpm, 6.8 bar IMEP) is a point of maximum efficiency for this engine. Finally, the high load/speed operating point (4500 rpm, 12.8 bar IMEP) is representative of maximum power operation.

Table 2: *Operating conditions used in the experiments.*

Operating points	OP 1	OP 2	OP 3
Engine speed [rpm]	4500	2000	1350
IMEP [bar]	12.8	6.8	2.8
Injected fuel [mg/cc]	28.4	15.3	8.4
λ [-]	1	1	1
EGR rate [%]	0	0	0
Spark Timing [CAD BTDC]	10	11.8	22
Intake pressure [bar]	1.1	0.68	0.39
Exhaust pressure [bar]	1.07	1.04	1.01
Coolant and oil temperature [K]	363	360	360

An internally developed software was used for combustion diagnostics [33, 34]. This tool uses a thermodynamic model to calculate the cycle-averaged values of several combustion-related parameters from the measured in-cylinder pressure signal. The Heat Release Rate (HRR) was calculated by performing an energy balance of the system based on the first law of thermodynamics. The complete details of the hypothesis, models, submodels and equations implemented in this software can be found in previous publications from the literature [35, 36].

$$HRR = mc_v\frac{dT}{d\alpha} + \frac{dQ}{d\alpha} + P\frac{dV}{d\alpha} - (h_{f,inj} - u_{f,g})\frac{dm_{f,ev}}{d\alpha} + RT\frac{dm_{bb}}{d\alpha} \quad (1)$$

Equation 1 shows the resulting expression for calculating the HRR. In this equation m is the instantaneous mass calculated from the trapped mass at the Intake Valve Closing (obtained by means of a filling and emptying submodel implemented in the software) and taking into account the accumulated blow-by leakage. c_v is the specific heat, calculated taking into account the instantaneous temperature and composition of the charge (this value was not fixed). T is the gas temperature, P is the pressure and Q represents the heat transfer to the chamber walls. R is the gas constant and m_{bb} is the blow-by mass. The term $(h_{f,inj}\text{-}u_{f,g}).dm_{f,ev}$ represents the

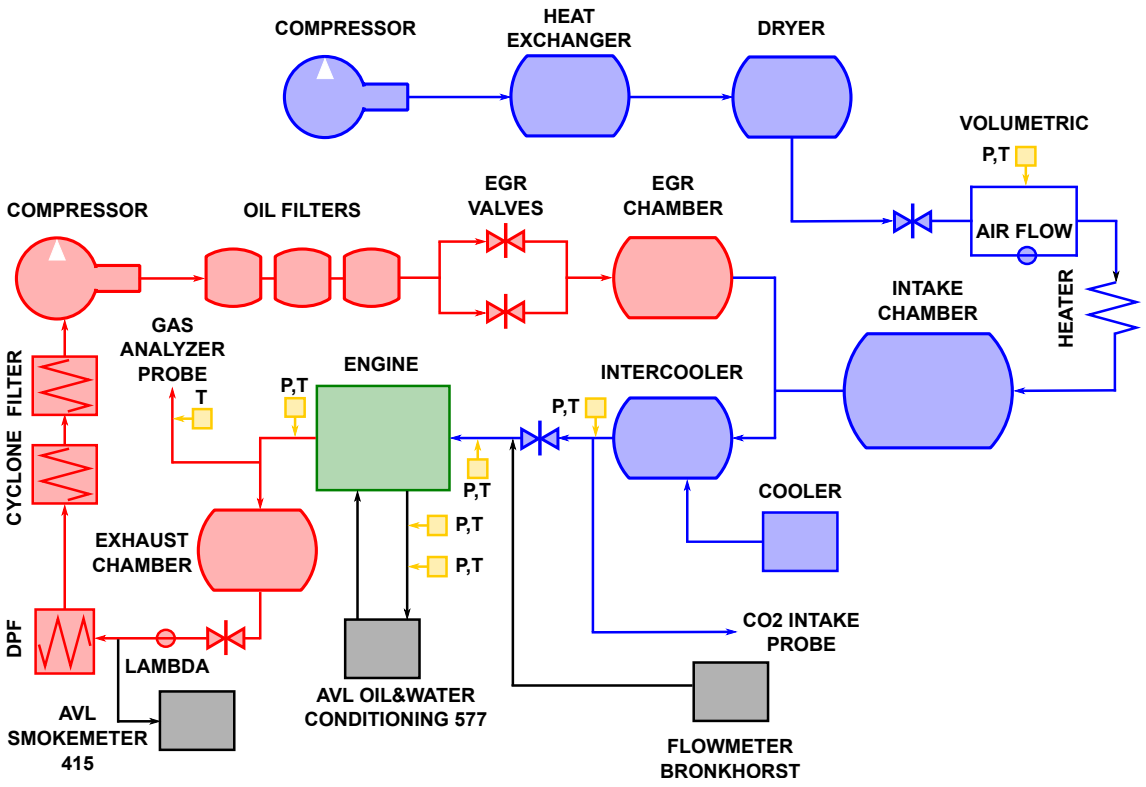

Figure 1: *Layout of the test bench.*

flow work of the injected fuel, evaporation and heating up to the gas temperature. However, as this engine was port fuel injected, this term was null.

2.2. Numerical model

The CFD simulations were carried out using the commercial code CONVERGE [37], a CFD software based on the finite volume method and developed specifically for Internal Combustion Engine (ICE) applications. The complete details of the physical and numerical models used for the calculations are described in previous investigations [30, 38].

A sketch of the computational domain is shown in Fig. 2, including a detailed view of the mesh inside the pre-chamber. Due to certain design restrictions of the cylinder head, the pre-chamber is not centered in the main combustion chamber, and it has an offset with respect to the cylinder axis. Table 3 presents a summary of the meshing strategies adopted for this model, highlighting also the criteria for using the Automatic Mesh Refinement (AMR) algorithm to improve grid resolution in run-time [37].

Regarding the turbulence modeling, the simulations were carried out in an unsteady Reynolds-averaged Navier–Stokes (URANS) framework. A two-equation turbulence model (RNG k-ϵ model) was used to estimate the Turbulent Kinetic Energy (TKE) generation in the cylinder and the dissipation of this energy (ϵ). This model has been widely used in ICE simulations [39, 40].

Table 3: *Mesh details.*

Computational region	**Cell size**
Intake port	2 mm
Exhaust port	2 mm
Cylinder	1 mm
Cylinder walls/Piston/Valves	0.5 mm
Pre-chamber	0.25 mm
Pre-chamber walls & holes	0.125 mm
Spark plug gap	0.0625 mm
AMR sub-grid criteria	**Minimum cell size**
Temperature: 2.5 K	0.125 mm
Velocity: 1 m/s	0.125 mm

The combustion process was modeled with a two-zone flamelet based model. The extended coherent flamelet model (ECFM) [41, 42] uses the flame surface density (Σ) to track the position of the flame front. Thus, an additional transport equation for Σ is solved instead of detailed chemistry calculations, reducing the associated computational time. Other phenomena related to the flame stretching by turbulence, thermal expansion and the dilation of the flow are also accounted for with this model [43, 44]. The resulting flame front is used to divide the computational domain into burned-/unburned regions by large scale stratification of species. This model is well-suited to describe the combustion process of SI engines [45]. Moreover, the ECFM model has an integrated Imposed Stretch Spark Ignition Model (ISSIM) for simulating

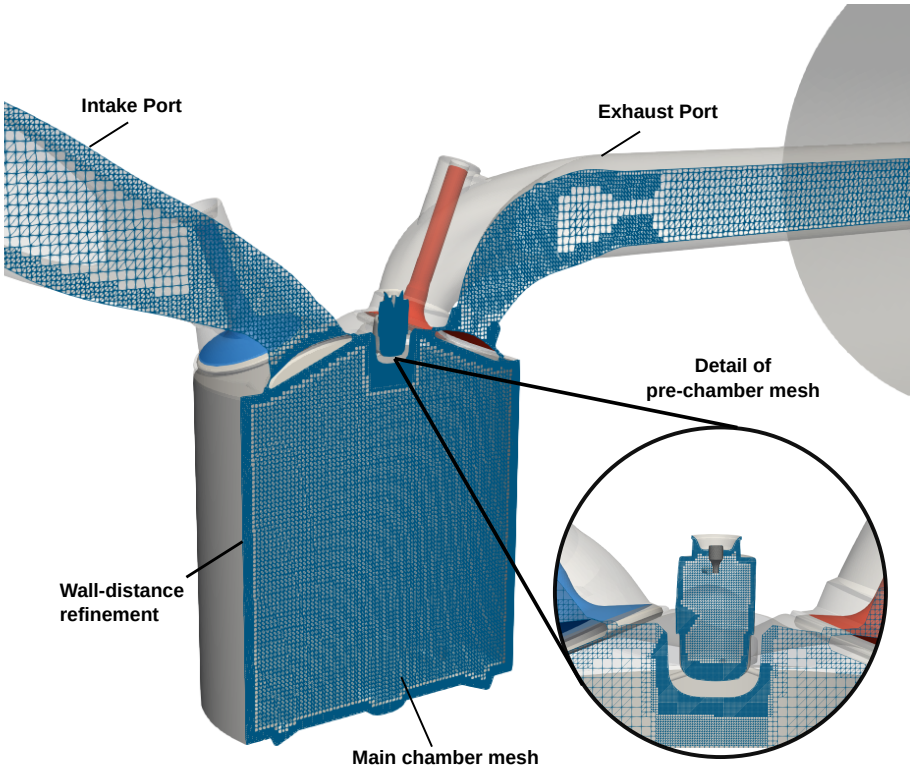

Figure 2: *Computational domain and mesh details.*

the electrical circuit of the spark plug [46, 47]. This model transforms an energy input into an initial flame surface density to start the propagation of the flame.

In order to account for the thermo-chemical properties of the flame (flame thickness and laminar flame speed) and knocking combustion (auto-ignition), the ECFM model requires tabulated values. Thus, a 0D well-stirred reactor model (for the ignition delay data) and 1D laminar flame speed calculations were used to generate the data tables of the flame properties for several combinations of temperature, pressure, equivalence ratio and mixture composition. These calculations are better described in a previous research [30]. Fig. 3 shows a set of results for both the laminar flame speed and auto-ignition delay at high pressures (more representative of engine-like conditions). Here, several reaction mechanisms [48, 49, 50, 51, 52] are compared with experimental data [53, 54]. Furthermore, the mechanism from Liu et al. [48] was selected to generate the data tables as it gave the most accurate predictions.

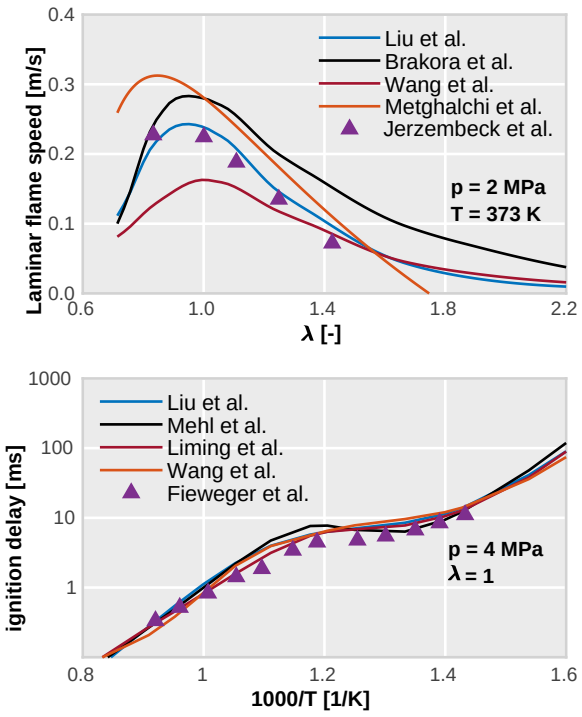

Figure 3: *Auto-ignition delay and laminar flame speed validation for different gasoline surrogates mechanisms at engine-like conditions.*

2.3. Validation of the CFD model

Before analyzing the simulation results, the validation of the CFD model is a fundamental step to assure a high reliability of the numerical solution. For this purpose, the operating points described in Table 2 were considered. The measurement methodology and protocols are widely explained in previous research works from the authors [24, 32]. This methodology consisted in adjusting the injected fuel mass to

obtain the target Indicated Mean Effective Pressure (IMEP) operating with the conventional SI system, and keeping it constant for the subsequent pre-chamber tests. Thereafter, a Spark Timing (ST) sweep was performed until reaching Maximum Brake Torque (MBT) conditions, or by contrast, until a continued ST advance was prevented due to knocking combustion. The geometric definition of the pre-chamber was kept constant in all tests, with the geometrical parameters shown in Table 4. All the tests were performed at stoichiometric conditions without EGR dilution.

Each CFD simulation was configured and initialized with the corresponding experimental data (intake/exhaust temperatures, intake/exhaust pressures, injected fuel mass, spark timing...). The lumped model proposed by Torregrosa et al. [55] was used to estimate the wall temperatures for the piston, liner and cylinder head, from the experimental data in each operating point. After the simulations ended, the in-cylinder pressure and heat release rate were compared to those measured in the single cylinder engine. Results of this comparison are shown in Fig. 4, where the in-cylinder pressure data, averaged over 250 measured cycles, and the HRR, estimated from the pressure signal in the main chamber, are included for each operating point. A very good agreement can be observed between the experimental and simulated pressure traces of the three tested conditions. Additionally, the HRR traces are also fairly reproduced by the CFD model in terms of ignition onset, maximum combustion rate and combustion duration.

In order to validate the robustness of the model, Table 5 presents a comparison of the IMEP and indicated efficiency values. Results show that both indicated parameters match very well between experiments and simulations. Therefore, these calculations can be used to analyze in depth the physical and thermo-chemical processes involved in this ignition strategy.

Table 4: *Baseline pre-chamber geometry definition.*

ID	PC1
Volume [mm^3]	600
Number of holes	6
Hole diameter [mm]	0.7
A/V ratio [1/m]	3.9
Protrusion into the main chamber [mm]	5

Table 5: *Validation of indicated parameters.*

Operating point	IMEP [bar]		Indicated eff. [%]	
	Experimental	Simulated	Experimental	Simulated
OP 1	12.8	12.87	43.4	43.5
OP 2	6.8	6.78	41.5	41.4
OP 3	2.8	2.83	36.0	36.2

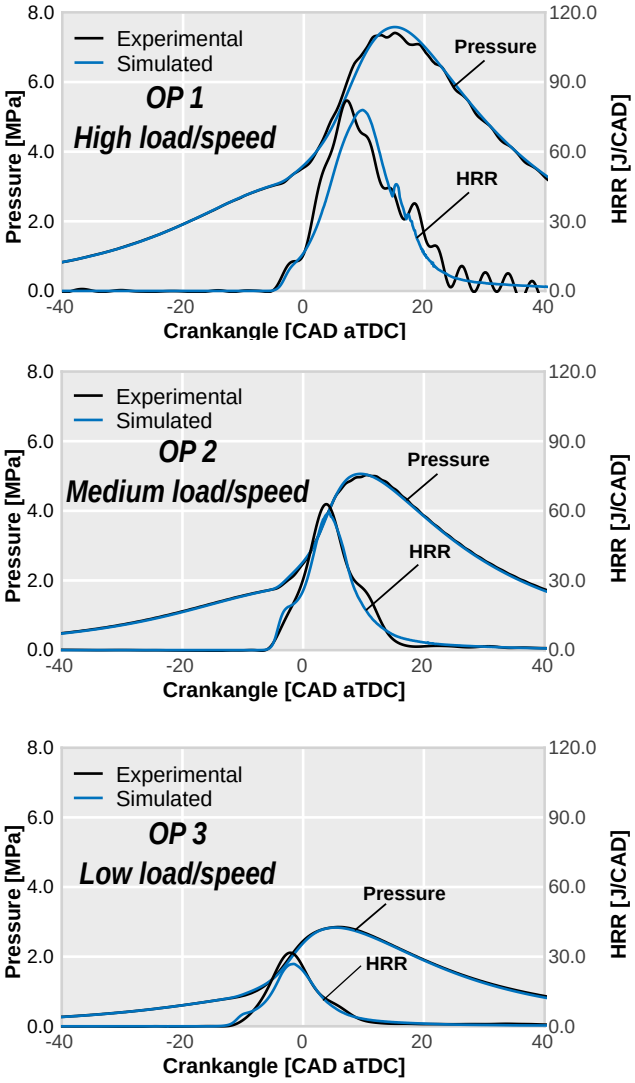

Figure 4: *CFD model validation for different operating points.*

2.4. Methodology

A well-structured methodology is required to gain knowledge of the performed calculations. Since there are limited studies comparing the passive pre-chamber ignition concept under different engine load/speed conditions by advanced numerical simulations [56, 57, 58], a detailed analysis of the relevant physical processes involved in this combustion system must be made. Therefore, the comparison between the simulated conditions was divided in two parts. The first part was focused on the pre-chamber. Here, the most relevant aspects of the combustion process, mixture stratification and turbulence field inside this region were studied. Moreover, an energy balance was performed to understand how the concept is taking advantage of the energy available for igniting the main chamber. The second part of this study focused on the main chamber combustion and characteristics of the jets. In this stage, a spatial analysis was performed to understand

how the combustion process evolves inside the main chamber and the impact of the jets over the global performance of the engine.

After analyzing the differences between the 3 simulated operating points, a detailed study of the low engine load/speed point was made. A recurrent issue reported in the literature for this operating condition is the inability to delay the spark timing towards the expansion stroke, for achieving higher exhaust temperatures. Furthermore, a spark timing sweep was performed with the calibrated CFD model from the MBT spark timing to the most delayed spark timing reached in the experimental campaign. An additional simulation with the spark triggered at TDC was also performed to better understand the general trends related to the aforementioned issue. In this case, the combustion process and energy conversion inside the pre-chamber were deeply analyzed, highlighting important aspects related to the ejection process as the spark is triggered closer to TDC. Finally, the impact of these changes over the evolution of the main chamber combustion was also studied.

3. Results and discussion

This section shows the results obtained after applying the described methodology. Also, the observed trends are widely discussed, starting form the analysis of the passive pre-chamber concept at different operating points and then, moving towards the detailed study at low load/speed conditions.

3.1. Characteristics of the passive pre-chamber concept in different operating points

A broad analysis was performed with the calibrated models shown in Fig. 4. These simulations will help to understand key aspects of the passive pre-chamber concept, that could allow to propose alternatives for improving the performance of this ignition system and overcome the issues encountered in the literature at low engine load/speeds.

3.1.1. Analysis of the pre-chamber combustion

The first stage of this investigation focused on analyzing the pre-chamber combustion process. The most relevant parameters of this process are shown in Fig. 5. The nomenclature for the simulated operating conditions was shown in Table 2, where OP 1 corresponds to high engine load/speed conditions, OP 2 corresponds to medium load/speed conditions and OP 3 corresponds to low load/speed conditions. Each simulation was launched with the corresponding experimental MBT spark timing, which is highlighted by vertical lines in Fig. 5, with the same color as the corresponding curve.

The top graph of Fig. 5 depicts the chemical HRR profiles inside the pre-chamber, computed directly by the CFD model from the species transformation along the combustion process. Significant differences are observed between the three operating points in both maximum combustion rate and combustion duration. These effects can be attributed to two main aspects: the difference in fuel mass available inside the pre-chamber at the spark timing, and the local flow conditions. The flame propagation inside the pre-chamber not only depends on the amount of energy available but also on how efficiently that energy is released. Therefore, the mixture stratification and turbulence field play an important role on the performance of the concept. Another interesting trend is the secondary heat release peak, caused by the back-flow coming from the main chamber after pressure increases due to the main combustion process. Moreover, the relevance of this secondary HRR peak increases as the engine load/speed decreases. While the back-flow HRR peak is similar to the primary one at medium load/speeds, it becomes even higher than the first HRR peak at low load/speed conditions. The relationship between both peaks depends on both the amount of unburned mixture injected back into the pre-chamber and the fuel remaining in this region at the beginning of the back-flow.

The middle and bottom graphs of Fig. 5 show the pressure difference between the pre-chamber and main chamber (Δp) and the jet momentum, two representative parameters of the ejection process. Both curves follow the same trend as the corresponding HRR profiles. As the combustion rate decreases (i.e. at low engine load/speed), the pressure increase inside the pre-chamber is gradual, affecting the ejection. The jet momentum flux, calculated as the product of the flow rate and the flow velocity through the holes, is proportional to the pre-chamber pressurization. As it can be seen, the maximum momentum achieved for medium load/speed conditions is four times lower than the momentum peak of high load/speed conditions. Moreover, the momentum at low engine load/speed conditions is over ten times lower than the high load/speed case.

This analysis leads to the first important difference between the studied operating points. Given that the jet features are considerably deteriorated at low load/speed conditions, the concept loses its performance when operating in this point.

In order to gain further insight, a detailed analysis of the internal flow field and energy conversion inside the pre-chamber was performed. The top plots of Fig. 6 show the evolution for the Residual Gas Fraction (RGF) and Turbulent Kinetic Energy (TKE) averaged in the pre-chamber region against the crankangle.

Here, the deterioration of the flow conditions as the engine load and speed decrease is clearly observed. The RGF, included on the left side, gives an overview of the pre-chamber scavenge. At high load/speed conditions the percentage of residual gases that remain inside the pre-chamber from the previous cycle is in the range of 15% to 8% between -40 and 0 CAD after top dead center (aTDC). However, the RGF increases significantly when moving to lower engine load/speeds. In the case of OP3, the residual gas fraction ranges from 30% to 20% in the same time interval considered before. The visualization of the spatial distribution of RGF for each operating point at -20 CAD aTDC reveals that this situation is even worse when considering the local stratification of resid-

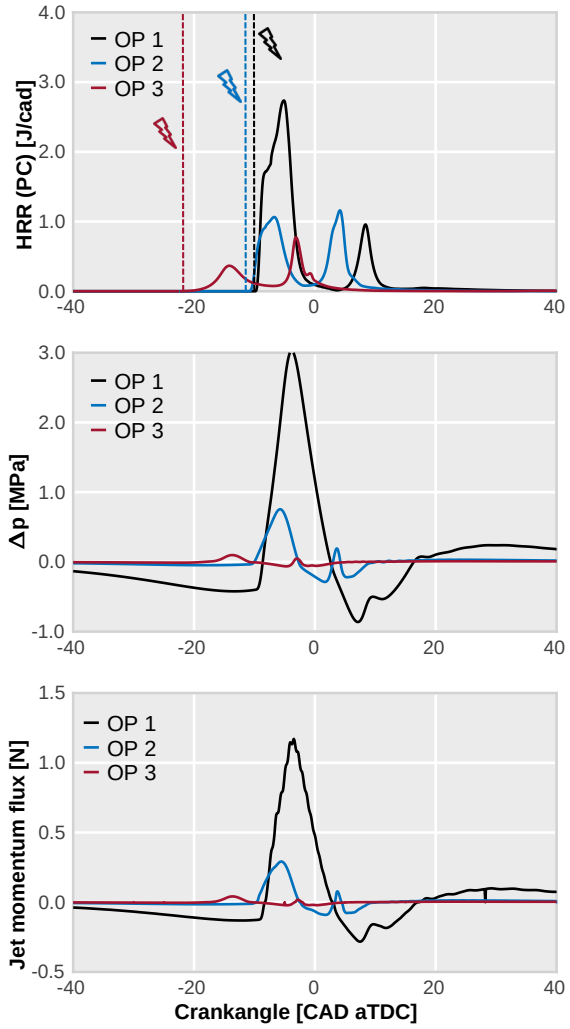

Figure 5: *Pre-chamber combustion parameters for each operating point. The HRR trace, pressure difference between the pre-chamber and main chamber (Δp) and jet momentum are plotted.*

ual gases. The high percentage of RGF located at the spark plug gap compromises the initial flame development. This finding matches the results presented in previous studies by the authors [24, 38], where the high sensitivity of the laminar flame speed to the residual gases dilution was shown. Therefore, the inherent increase in RGF when operating at low load/speed conditions is a factor that strongly limits the generation of high-quality jets and subsequently, the performance of the concept.

On the other hand, the generation of turbulence is also an important aspect in premixed combustion. The plot located at top-right side of Fig. 6 shows the average TKE inside the pre-chamber. These levels are almost eight times higher for OP 1 than those of OP 3, favoring the flame propagation while generating higher pressure difference among the pre-chamber and main chamber. The snapshots included in the bottom part of this plot show the spatial distribution of TKE in the pre-chamber at -20 CAD aTDC. The turbulence flow pattern is very similar between the three cases. The intense TKE levels are generated at the pre-chamber bottom due to the flow stretching through the holes. This pattern indicates that the turbulent kinetic energy is rapidly dissipated as the flow moves to the spark plug location. This is more evident at low engine load/speeds, since the TKE generated is extremely low, hindering the final stages of the flame propagation inside the pre-chamber.

Moving on, analyzing the energy conversion inside the pre-chamber, the top graph of Fig. 7 shows the fuel mass available within this region as it is filled during the compression stroke. As it can be seen, the amount of fuel inside the pre-chamber depends on the engine load. Since the fuel per cycle is lower for OP 3, the pre-chamber is filled with less fuel when operating at lower engine load/speeds (see Table 2). This effect is even more critical when the spark timing needs to be advanced to achieve an optimum combustion phasing. For example, OP 1 has a spark timing of -10 CAD aTDC whereas OP 3 triggers the spark at -22 CAD aTDC. Consequently, the fuel available within the pre-chamber as the spark timing moves to the bottom dead center (BDC) is reduced, compromising the performance of the concept.

However, this aspect is not the only contributing factor for obtaining suitable jets for the main chamber ignition. How this energy is consumed and how much of it ignites the main chamber are two relevant aspects as well. The middle and bottom graphs of Fig. 7 show the energy balance inside the pre-chamber during the ejection process. In this figure, the absolute energy values are plotted in the middle graph and the relative share of each parameter with respect to the total energy available at the start of combustion are shown at the bottom.

In the top graph, the full length of the bars represents the energy available at the beginning of the combustion process. In each bar, the red block corresponds to the energy used for effectively igniting the main chamber (Energy Available for Ejection, EAE), coming from the hot products ejected from the pre-chamber. The orange block is the energy losses due to heat transfer through the pre-chamber walls. The yellow block represents the unburnt fuel remaining in the pre-chamber at the end of ejection. And finally, the blue block is the energy lost during the ejection of non-reacting flow. In this last contribution, the flow is pushed towards the main chamber due to the pressure increase inside the pre-chamber, but the flame front has not reached the holes yet.

The EAE is computed by integrating the pre-chamber HRR from the start of combustion until the end of ejection. The pre-chamber heat losses were estimated with Angelberger's model [59], also computed between the start of combustion and the end of the ejection process. The unburnt energy remaining in the pre-chamber was calculated by multiplying the fuel mass inside the pre-chamber at the end of ejection by the Lower Heating Value (LHV) of the fuel. Finally, the fuel lost due to the inert ejection was calculated considering

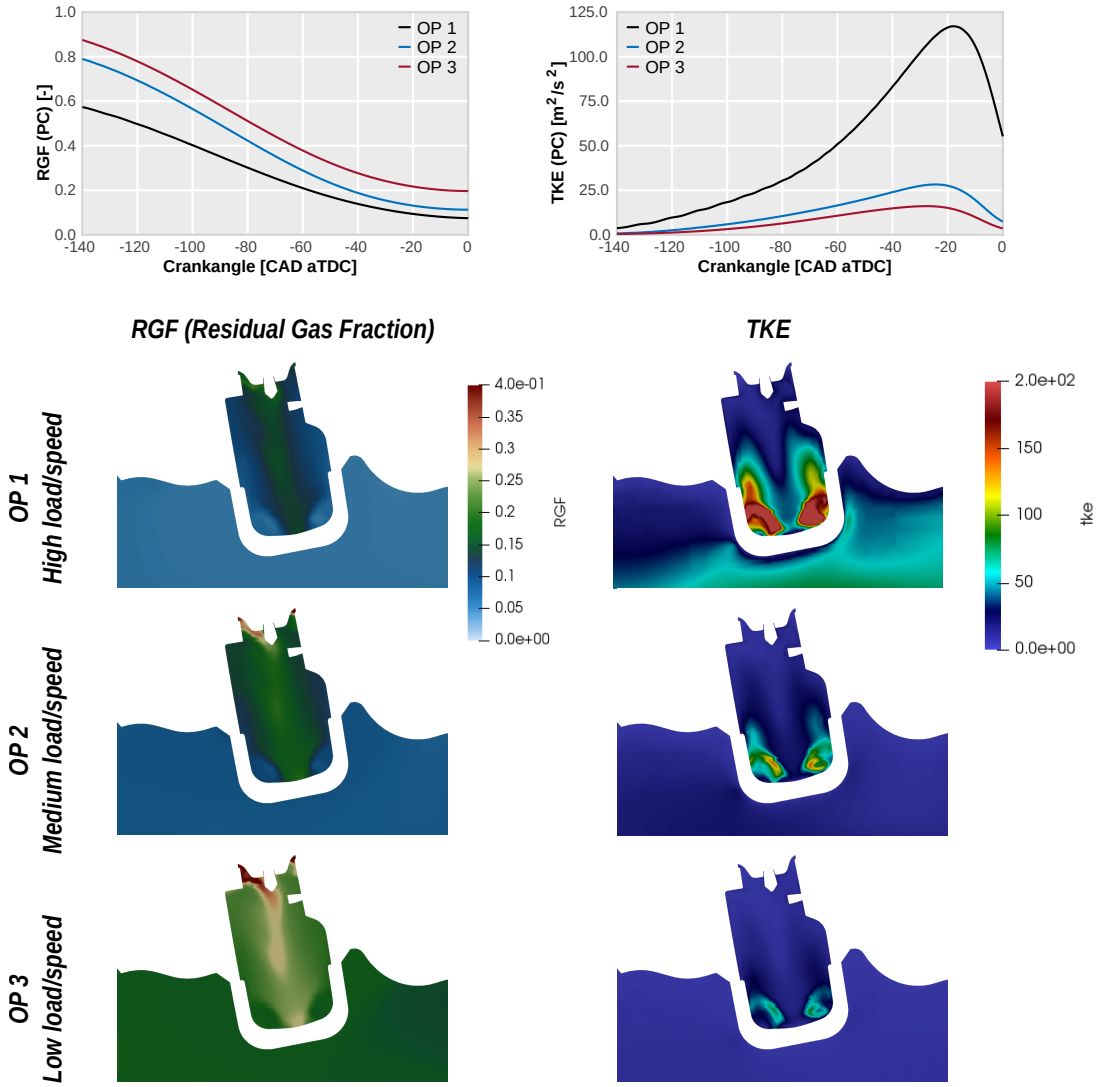

Figure 6: *Flow field characteristics inside the pre-chamber region. The average residual gas fraction and turbulent kinetic energy are plotted. Local distributions of both parameters at -20 CAD aTDC are also included.*

an integration surface at the exit of each hole. All unburnt fuel species flowing through these surfaces were computed from the start to the end of the ejection.

Inspecting the middle graph of Fig. 7, the absolute energy difference between the three studied cases is clearly observed. In addition, OP 1 not only has the most energy available, but also it is the most efficient in terms of energy conversion. The bottom graph of this figure shows that over 70% of the energy is used for igniting the main chamber. This is attributed to the high combustion rates achieved inside the pre-chamber in this operating point. The enhanced flow conditions (higher TKE and less residuals) allow the flame front to quickly sweep the entire volume, promoting an early ejection of reactive flow. Nevertheless, the share of heat losses is also the highest (8%), due to the high temperatures reached during combustion. In this case, the share of unburned fuel left in the pre-chamber is negligible, and the energy lost in inert ejection is less than 20% of the total energy.

Regarding OP 2, only 55% of the total energy is used for main chamber ignition. The unburned fuel remaining at the end of ejection increases up to 8%, indicating a lower combustion efficiency. Additionally, the share of heat losses (4%) is lower compared to OP 1. Nevertheless, the most significant difference comes from the ejection of inert gases: 33% of the fuel is ejected in these conditions. This is mainly due to the longer time it takes for the flame to reach the bottom of the pre-chamber, since the local conditions are worse in this particular operating point.

Analyzing the energy balance of OP 3 reveals that only 45% of the energy is used for igniting the main chamber, thereby 55% of the energy is lost in the other processes. The combustion rates of this operating point are slower due to unfavorable conditions inside the pre-chamber, resulting in 33% of the fuel to be left unburned at the end of the ejection. The increase of unburned fuel as the engine load/speed decreases confirms the aforementioned discussion related to the

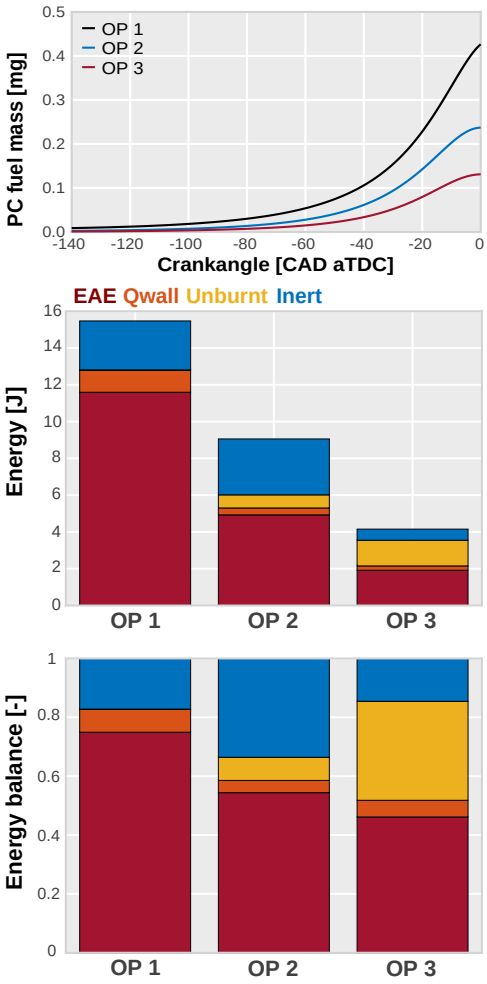

Figure 7: *Energy conversion inside the pre-chamber region during the ejection process.*

secondary HRR peak (see Fig. 5 for reference). The more fuel remaining inside the pre-chamber after the ejection ends, the higher will be the HRR peak during the back-flow, relative to the main HRR peak of the first combustion process.

3.1.2. Analysis of the main chamber combustion

The second stage of this research focuses on understanding the ignition and combustion process in the main chamber. Fig. 8 presents a summary of the main chamber combustion parameters. The top-row graphs of Fig. 8 show the HRR profile for each operating point in black color. Additionally, the HRR was divided into two contributions: the red line represents the amount of energy that is released within the jet boundaries, while the blue one shows the energy consumed outside the jets. Despite the expected differences in magnitude, the distribution among the energy released in-out the jets is similar for the three operating points. Most of the fuel is burned outside the jet limits. As the studied cases use non-diluted stoichiometric conditions, thermo-chemical properties of the mixture are favorable for sustaining the flame propagation, even in a low turbulence environment (outside the jets). Therefore, once the flame reaches the jet boundaries, it propagates freely as a regular SI engine flame front [30] at reasonable speeds.

Fig. 8 also shows the distribution of the energy consumption through the combustion chamber, in order to better understand the influence of the jets over the global combustion process. The polar graphs were computed by dividing the main chamber into six sectors, which corresponds to each pre-chamber jet. The sketch located at the bottom of Fig. 8 shows a graphic representation of this distribution. Here, each sector is labeled with the corresponding jet.

The first row of polar graphs shows the percentage of energy released in each sector with respect to the total energy released in the main chamber. The spatial pattern is quite similar in the three cases, where over 50% of the energy is consumed by jets 5 and 6, while the other 50% of the energy is equally divided in the rest of jets. This can be explained by the particular position of the pre-chamber in the combustion chamber. This element is not centered due to some design restrictions of the cylinder head. Consequently, jets 5 and 6 have a longer free path to penetrate in this region, allowing them to sweep a larger part of the main chamber volume.

The second row of polar graphs divides the percentage of energy released in each sector into the contribution inside and outside of the jet boundaries. The small share of energy released within the jets can be observed again in this representation. Moreover, the energy share between inside/outside of jets 2 and 3 is similar for OP 1. Nonetheless, the difference between the fuel burned inside and outside of these jets widens for OP 2 and OP 3.

Another clear trend is the reduction of the orange region size when moving towards lower engine load/speeds, indicating that the jets have less impact over the main chamber combustion process. The final row of polar graphs was computed to further quantify this aspect. These plots show the percentage of energy consumed inside and outside the jets, relative to the total energy of the corresponding sector. In OP 1, over 40% of the energy released in sectors 2 and 3 is consumed inside the jets, since they are closer to the chamber walls. On the other hand, jets 5 and 6 only burn 24% and 19% of the respective energy released in those sectors. These percentages are even lower for OP 2 and OP 3, ranging from 13% to 18%. Nevertheless, the relative trend is maintained in all operating points; the highest percentage of energy burned inside the jets corresponds to sectors 2 and 3, while the lowest one corresponds to sectors 5 and 6. In particular, jet 6 burns only 13% of the energy released in that sector at OP 3.

In order to gain additional insight on the flame evolution in the combustion chamber, an analysis of the jets penetration was performed. Only jet 6 was considered for this study, since it has the longest free path within the main chamber. With the purpose of establishing the jet boundaries, a user-defined function was programmed into the CFD code. This function initializes a passive species uniformly in the whole pre-chamber region at the beginning of the ejection process. This is a species that is transported with the flow but is not considered for the resolution of the governing transport

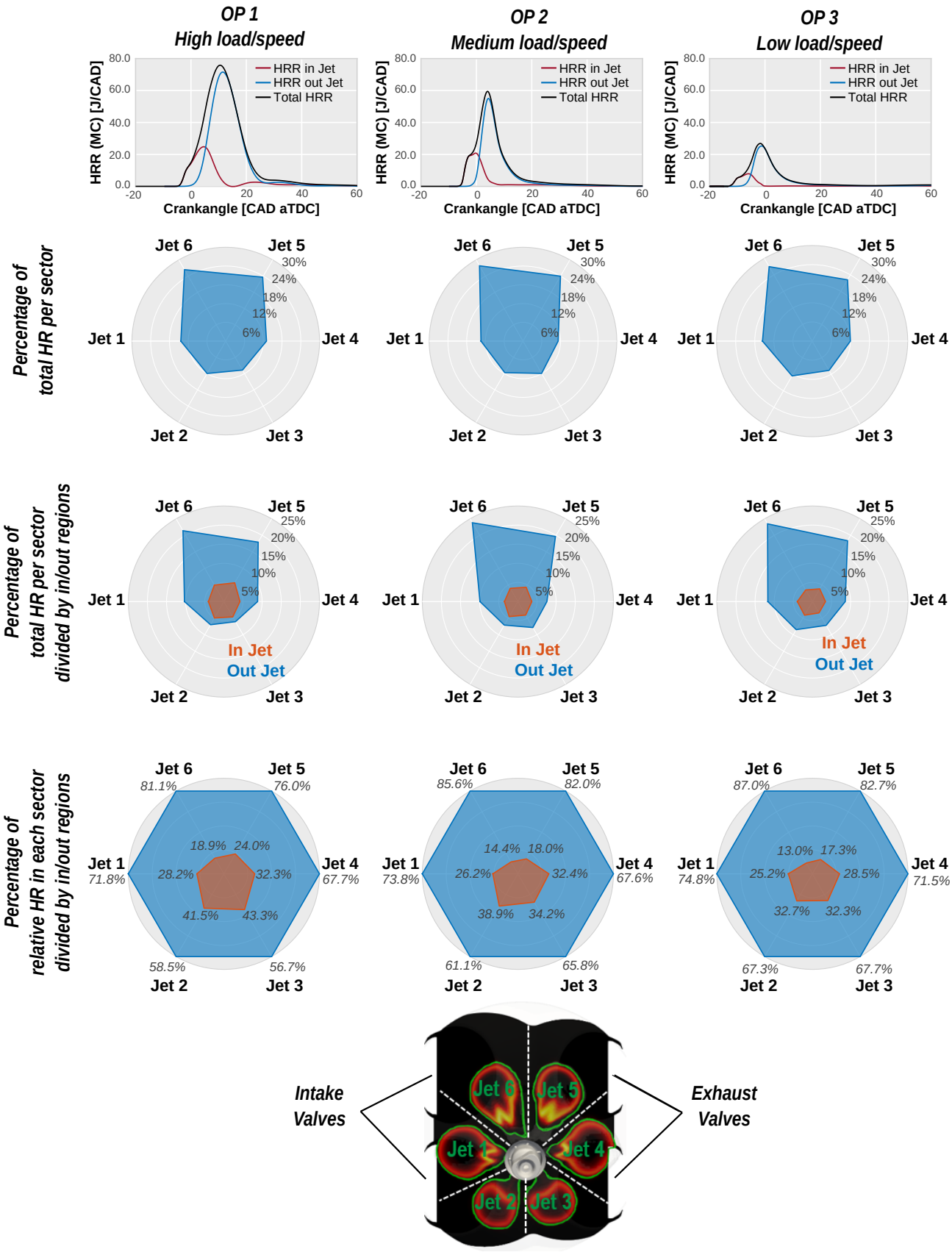

Figure 8: *Main chamber combustion for each operating point. The total HRR profiles are plotted in the top row along with the amount of energy that is consumed inside/outside the jets. The polar graphs show the amount of fuel consumed in each sector of the main chamber by a specific jet. The bottom plot sketches the division of the combustion chamber for computing the polar graphs.*

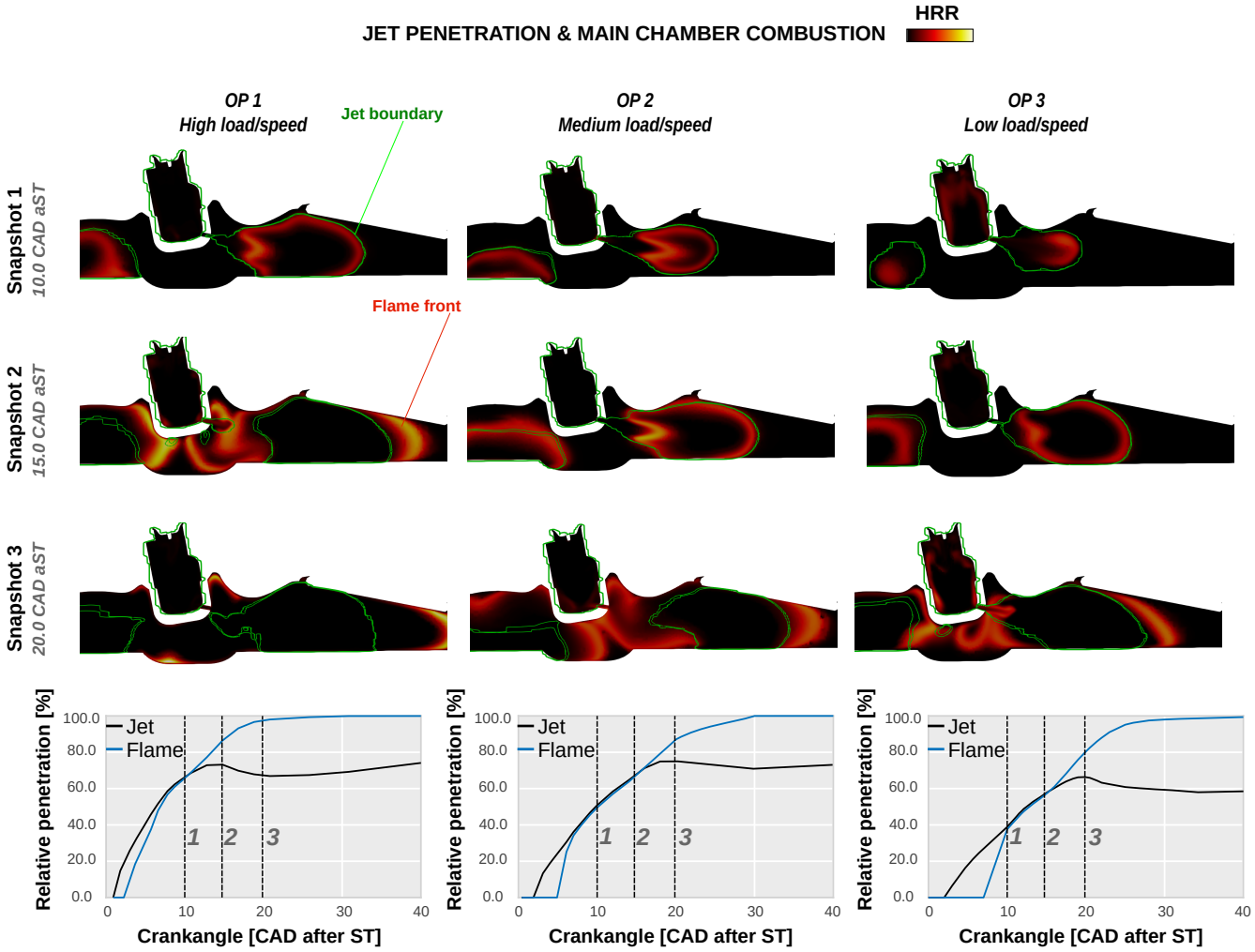

Figure 9: *Main chamber combustion and penetration of the jet/flame with the longest free path (jet 6). The local HRR is used to track the position of the flame at a given snapshot whereas the limits of the jets are determined with the help of a dynamic tracer and highlighted in green.*

equations (a dynamic tracer). The passive species is initialized to a value of 1 in the pre-chamber, and as the ejection progresses, fractions of that species start to penetrate into the main chamber. This allows to make the distinction between the mass coming from the pre-chamber and the mass that is burned in the main chamber. The threshold for defining the boundary of the pre-chamber jets is con-sidered to be 1/1000 of the dynamic tracer's mass. This threshold has been widely used in the literature for Diesel sprays, and was found to be an appropriate value for the turbulent jets coming from the pre-chamber.

Fig. 9 shows a snapshot sequence for a cut plane located in the axis of jet 6. The chosen snapshots correspond to three different crankangles, 10, 15 and 20 CAD after the spark timing of each individual case (CAD aST). To track the position of the flame front, the local HRR is plotted. The jet boundaries are stressed in green. Additionally, the relative penetration of the jet and the position of the flame, with respect to the maximum wall distance, are plotted at the bottom of Fig. 9. The vertical lines labeled by 1, 2 and 3 identify the crankangle of each snapshot.

Examining the slope of each curve reveals that the highest penetration rate is achieved at OP 1. In this case, the flame surpasses the jet limits and reaches almost 90% of the wall distance only 15 CAD after the spark timing. For OP 2 and OP 3 the penetration rate is lower, and the flame reaches the jet limits at later stages. Moreover, although the maximum jet penetration reaches almost 80% in OP 1 and OP 2, it stagnates around 60% of the wall distance in OP 3. This has relevant implications for the performance of the concept, since the flame will need to sweep a larger section of the main chamber volume by itself without the support of the turbulence generated by the jets.

Moreover, there is a delay between the beginning of the jet penetration (inert/non-reacting ejection) and the start of the flame penetration (reactive ejection). This gap increases

as the engine load/speed decreases due to the worsened flow field conditions inside the pre-chamber, which compromises the flame propagation and subsequently the ejection process.

The two main ideas extracted from this section can be summarized as:

- The relevance of jet features for improving the main chamber combustion, which depends on the pre-chamber burning rates and the pre-chamber energy management.
- The location of the pre-chamber inside the combustion chamber has a considerable impact on the distribution of energy in the main chamber. An asymmetrical position, where the pre-chamber is offsetted with respect to the cylinder center, has significant implications as some of the turbulent jets are not able to reach the chamber walls. In this situation, the turbulence generation is lower, and the flame will need to sweep a high percentage of the chamber volume without the aid of the jets.

Both aspects are critical at low engine load/speeds, since the inherent deterioration of the thermo-chemical and flow conditions in both chambers hinders the exploitation of the potential capabilities of the concept. This represents a major issue for implementing the passive pre-chamber system in production engines, given that the concept loses flexibility in this particular operating condition.

3.2. Exploring the limits of the concept at low engine load/speed conditions

A common trend found in previous experimental investigations performed by the authors [24, 32] was a huge increment of the cycle-to-cycle variations (CCV) as the spark timing is delayed at low engine load/speeds.

Fig. 10 shows the variability of the IMEP (σIMEP) and the exhaust temperature for the spark timing sweep performed in the real engine, operating with both conventional spark ignition and pre-chamber ignition. It is clearly observed how the pre-chamber concept maintains a suitable combustion stability with low levels of σIMEP throughout a wide range of spark timings. However, σIMEP suddenly increases after -10 CAD aTDC, reaching extremely high values.

This proves the high sensitivity of the passive pre-chamber ignition system to the spark phasing. Note that a variation of only 2 CAD is enough to reach the combustion instability threshold. Additionally, the exhaust temperatures are lower for the pre-chamber concept compared to the conventional spark plug, due to the higher burn rates achieved with the former ignition system. Thus, the spark must be triggered closer to TDC to obtain exhaust temperatures over 600K for the TWC warming up. In order to shed some light on the behavior of the concept when delaying the ST, the numerical model was used.

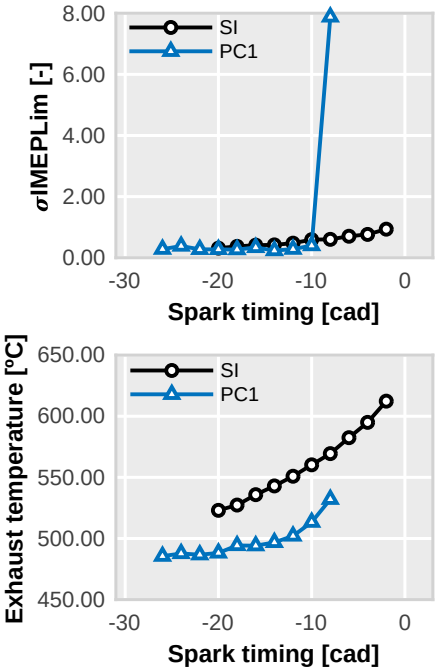

Figure 10: *Experimental spark timing sweep at low load/speed conditions. The variability of the IMEP (σIMEP) and temperature in the exhaust are plotted for both the conventional spark plug and pre-chamber spark plug at each spark timing.*

3.2.1. Spark Timing sweep analysis

Four simulations were performed with the calibrated CFD model in OP 3: the reference case with the MBT spark timing (-22 CAD aTDC) and three additional simulations with the ST triggered at -16, -8 and 0 CAD aTDC. The first three cases (ST-22, ST-16, ST-8), are also replicated in the test bench for validation purposes, being the case of the ST triggered at -8 CAD aTDC the threshold of combustion stability detected in the experiments. The conditions of the last case (ST TDC) were not reached during the experimental campaign due to the extreme CCV faced. However, this calculation can provide additional insight on the concept basis. All these simulations were setup considering the same configuration parameters (injected fuel mass, boundary and initial conditions).

Fig. 11 shows the experimental and numerical in-cylinder pressure traces. As it can be seen, the global trends are well captured by the CFD model, therefore, the calculations were used to study the performance of the concept by following the same methodology as the previous section.

Fig. 12 shows the HRR profiles inside the pre-chamber, the pressure difference with respect to the main chamber (Δp) and the momentum of the jets for each simulated case. Despite the small differences in the primary HRR peak of ST-22, ST-16 and ST-8 cases, the Δp and jet momentum follow a rising trend as the spark approaches TDC. The peak momentum achieved with the spark timing at -8 CAD is 50% higher than the reference MBT case (ST-22). This can be attributed to the higher fuel mass available at the start of combustion,

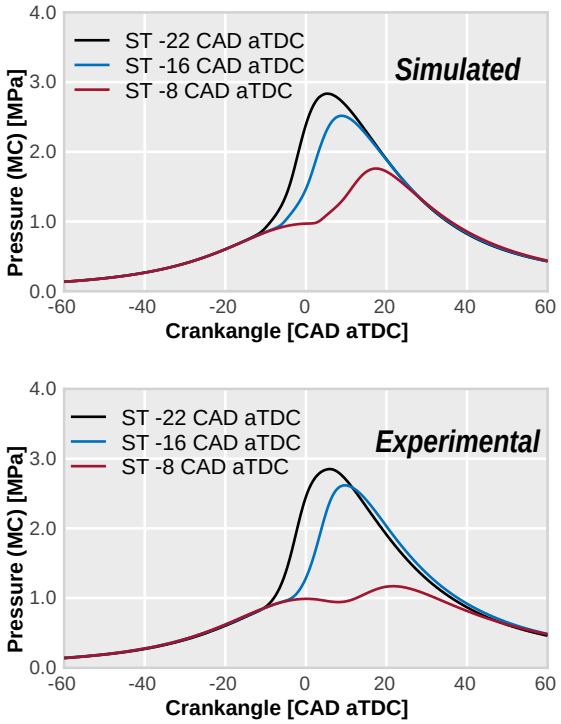

Figure 11: *Pressure profiles of the experimental spark timing sweep and the spark timing sweep performed with the calibrated CFD model at low load/speed condition (OP 3).*

since the pre-chamber is filled with additional flow when delaying the spark. Focusing on the simulation with the spark triggered at TDC, the combustion profile is considerably deteriorated, reaching a lower HRR peak and increasing the combustion duration. Nevertheless, the maximum momentum peak of this case is at the same level as the reference MBT spark timing.

In order to better understand these trends, the energy balance inside the pre-chamber during the ejection process was performed for each simulated ST and plotted in Fig. 13. Here, the same nomenclature of Fig. 7 was used.

From the top graph of Fig. 13 it can be seen that the absolute energy values increase as the spark timing is delayed, due to the extra filling of the pre-chamber. However, the levels of the effective energy used for igniting the main chamber (EAE) are kept within the same range for all the simulated cases. Inspecting the bottom graph shows that the percentage of EAE decreases as the spark approaches TDC, whereas the percentage of non-reactive ejected fuel mass increases. For the last simulation, with the spark triggered at TDC, over 50% of the energy is lost in inert conditions. Thus, the additional energy introduced in the pre-chamber by delaying the spark timing is not really harnessed. These trends can be attributed to two main factors: the worsening of the combustion process due to the lower TKE levels inside the pre-chamber, and the downward motion of the piston, which forces the gases to exit the pre-chamber prematurely during the first stages of the expansion stroke.

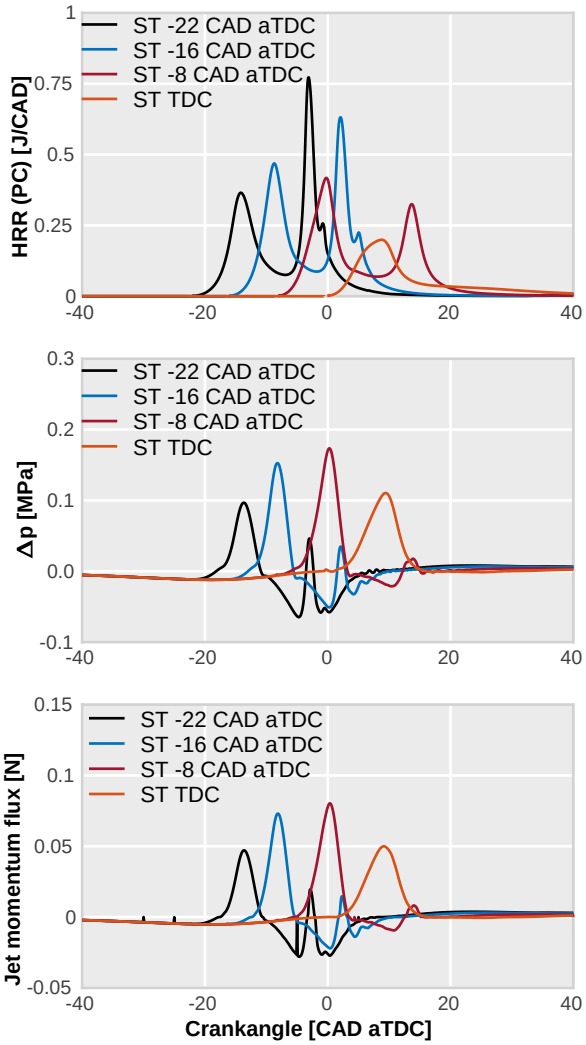

Figure 12: *Pre-chamber combustion parameters for each simulated spark timing. The HRR trace, pressure difference between the pre-chamber and main chamber (Δp) and jet momentum are plotted.*

The top plot of Fig. 14 shows a comparison between the real spark timing (*setting ST*), defined as the moment when the spark is triggered, and the *effective spark timing*, defined as the moment when the main chamber ignition occurs. The dashed diagonal line in this plot corresponds to the ideal scenario, where the main chamber ignition starts at the exact time when the spark is triggered. In reality, there is a delay between the triggering of the spark and the onset of the main chamber combustion. In particular, for the pre-chamber concept, the ignition can be characterized and divided into three stages: the onset of pre-chamber combustion, the beginning of reactive ejection (when hot gases start to penetrate towards the main chamber) and the onset of main chamber combustion. These stages are depicted in Fig. 14 for each simulated ST and, it can be appreciated how the gap between the stages widens as the spark timing is delayed. For the MBT case, there is a 9 CAD interval between the beginning of pre-

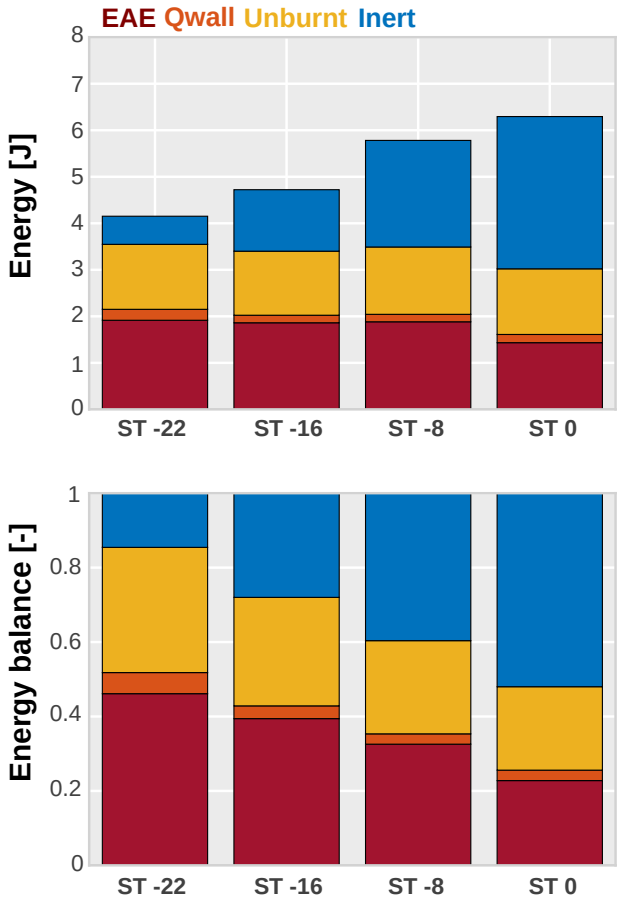

Figure 13: *Energy conversion inside the pre-chamber during the ejection process for the spark timing sweep.*

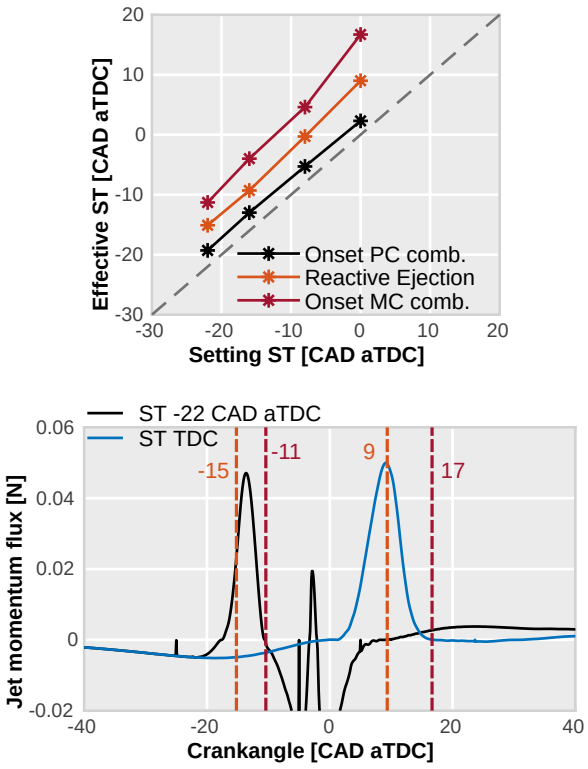

Figure 14: *Difference between the setting spark timing and the real spark timing, defined as the onset of the main chamber ignition.*

chamber combustion and the onset of main chamber combustion. On the other hand, for the most delayed ST simulation, the gap between these two events is over 15 CAD. Since there is a larger time interval between the spark timing and the start of main chamber combustion, the flow field between consecutive cycles may present higher variations in terms of thermodynamics and turbulence. Therefore, the ejection and combustion processes may face extremely different flow conditions between cycles, increasing the CCV.

The bottom graph of Fig. 14 shows the jet momentum profiles for the ST-22 and ST TDC simulations. Although the morphology of the curves is quite similar, an important difference is observed in the dashed lines that are drawn over each profile. These lines represent the crankangle at which the reactive ejection begins (orange) and the onset of main chamber combustion (red). The MBT simulation not only has a shorter time gap between these two events (4 CAD), but also the momentum is still increasing at the beginning of reactive ejection. Therefore, the concept is taking advantage of a higher jet momentum to ignite the main chamber while sustaining the flame in the initial stages of combustion. On the contrary, the reactive ejection does not begin until the peak momentum is reached in the ST TDC case. Thus, the initial stages of the main chamber combustion are sustained by a lower jet momentum and subsequently, by less turbulence. Additionally, the difference between the start of reactive ejection and the onset of main chamber combustion increases from 4 CAD to 8 CAD.

In order to better analyze these phenomena, Fig. 15 shows a snapshot sequence of the main chamber combustion considering both the MBT spark timing case (ST-22) and the most delayed ST simulation (ST TDC). Again, the local energy release is colored to track the flame evolution and the jet boundaries are highlighted in green. Comparing the snapshots 1 and 2, it can be seen that the jets are evolving similarly, although the reactive ejection is delayed when triggering the spark at TDC. Moreover, snapshots 3 and 4 of the MBT case show the flame front transformation form inside to outside of the jets. After reaching the jet boundaries, the flame front evolves as a conventional flame propagation. The ignition pattern for the delayed ST case is quite different, since only the mass entrained by the jets is consumed in the considered time frame.

This trend can be clearly observed in the right-side graphs of Fig. 15, where the HRR trace in the main chamber is drawn. The black curve represents the total energy released, while the red and blue curves represent the amount of fuel that is consumed inside and outside the jets respectively. The distribution of energy clearly changes among both considered cases. While only 20% of the energy is released inside the

jets for the MBT case, over 50% of the main chamber charge is consumed inside the jets for the delayed ST simulation. Thus, the performance of the jets plays a significant role in the main chamber combustion when the spark timing is delayed. This is even more critical at very delayed ST since thermodynamic and flow features worsen during the expansion stroke.

This study has demonstrated that increasing the jet momentum does not guarantee a performance improvement if most of this momentum is applied to non-reacting flow. Therefore, increasing the burning rates inside the pre-chamber to achieve an early reactive ejection while advancing the onset of main chamber ignition becomes crucial. However, achieving a high combustion rate inside the pre-chamber is complicated as the spark timing is pushed towards TDC.

Finally, Fig. 16 shows one of the main reasons why the HRR sharply decreases around TDC. In this figure the spatially-averaged turbulent kinetic energy inside the pre-chamber is drawn. A sharp decrease in the intensity of the turbulence is observed after -20 CAD aTDC, compromising the combustion in this region. This trend matches the pattern reported by the experimental results of Fig. 10, where the concept shows a high sensitivity to ST delaying in terms of combustion stability. Therefore, modifying the pre-chamber geometry for increasing the turbulence intensity may help to improve combustion stability and achieve high quality jets by sustaining fast burning rates even at delayed spark timings.

4. Summary and conclusions

In this paper, a state of the art numerical investigation was carried out to asses the performance of the passive pre-chamber ignition concept in a turbocharged gasoline SI engine for light duty applications. Three key operating conditions of the engine map were simulated and compared with a well-validated CFD model. Particularly, the low engine load/-speed operating point, a recurrent problematic condition found in other research works, was studied by performing a spark timing sweep with the numerical model.

The novel methodology developed in this research for analyzing the fundamental aspects of combustion and energy management of the passive pre-chamber ignition system, has allowed to close the knowledge gap between the physical characteristics of the concept and the issues encountered in the literature when operating at low engine load/speed conditions.

The most relevant findings of the performed simulations have allowed to fulfill the research objectives defined for this investigation. These findings can be summarized as follows:

- At high load/speed conditions, the passive pre-chamber concept is able to perform very well in terms of energy conversion and combustion. Over 70% of the energy available in the pre-chamber is used to initiate combustion in the main chamber. The favorable flow conditions in both chambers (low levels of residual gases and high generation of turbulent kinetic energy) help to promote the flame propagation during the pre-chamber combustion and the main chamber ignition.

- On the other hand, at low engine load/speed conditions, The inherent deterioration of the turbulent kinetic energy and the increased level of residuals inside the pre-chamber, compromises the performance of the concept. The pressurization of the pre-chamber is slower, thus, the jet features are worse and the main chamber ignition is delayed as a result of the slow combustion rates. Additionally, the energy management inside the pre-chamber is also worsened, leaving over 30% of the fuel in this region to be unburned at the end of the ejection.

- The relative position of the pre-chamber in the cylinder head has a significant impact on the heat release distribution along the main combustion chamber. The larger offset between the cylinder axis and the location of the pre-chamber, the more energy gradients will there be in the main chamber. In this situation, the relative penetration of some jets is lower due to the larger path to reach the cylinder wall. Therefore, a higher percentage of the main chamber volume needs to be swept by a conventional flame propagation without the support of the high turbulence levels generated by the jets. This fact becomes critical at low load/speed conditions, given that the momentum of the jets is lower due to the slower combustion process in the pre-chamber.

- The spark timing sweep analysis performed at low engine load/speed conditions revealed an energy management worsening inside the pre-chamber. Moving the spark timing towards the expansion stroke increases the energy available inside the pre-chamber, however, most of this energy is lost during the ejection of non-reactive flow. This fact widens the gap between the triggering of the spark and the ignition of the main chamber. Thus, increasing the burning rates inside the pre-chamber volume, to promote an early reactive ejection, is crucial for improving the main chamber combustion when delaying the spark timing.

- This last remark can be achieved by two alternatives. The first is to optimize the internal design of the pre-chamber in order to improve the scavenging of residual gases and increase the generation of TKE. The second alternative is to combine the passive pre-chamber concept with another state of the art strategy for accelerating the pre-chamber combustion process. One possibility is to heat the walls of the pre-chamber, by adding a special coating or by an electric resistance. This would subsequently increase the mean flow temperatures of the gases in this region to achieve higher laminar flame speeds. Another interesting idea is to add a high energy ignition system inside the pre-chamber (plasma, barrier discharge, surface discharge, corona igniter).

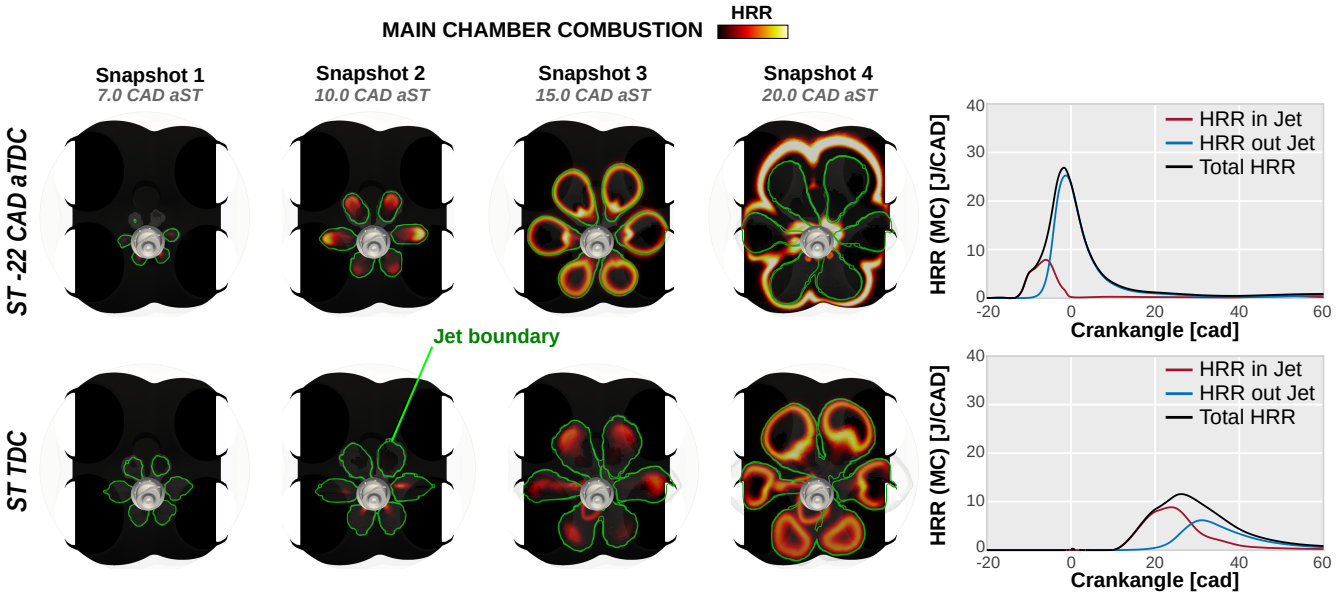

Figure 15: *Visualization of the main chamber ignition sequence for the MBT spark timing (ST -22 CAD aTDC) and the TDC spark timing (ST TDC). The local energy release is used to track the position of the flame whereas the limits of the jets are determined with the help of a dynamic tracer. The values and evolution of the HRR profiles inside/outside the jets for both cases are also included in the right-side graphs.*

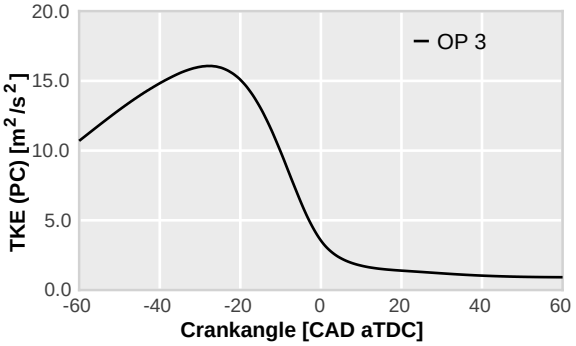

Figure 16: *Spatially-averaged turbulent kinetic energy inside the pre-chamber at low load/speed conditions.*

This would allow to burn the pre-chamber charge very quickly, acting similarly to an active pre-chamber system.

The findings of this investigation have improved the knowledge on the underlying physics of the passive pre-chamber ignition concept. This can be considered as an initial step towards implementing this technology to production engines. However, additional experimental and numerical studies must be carried out to evaluate the alternatives proposed to overcome the issues found in this and previous investigations at low engine load/speed conditions.

Acknowledgements

The authors want to express their gratitude to CONVERGENT SCIENCE Inc. and Convergent Science GmbH for their kind support for the 0D, 1D and CFD calculations with the CONVERGE software.

The work has been partially supported by the Spanish Ministerio de Economía y Competitividad through grant number TRA2017-89139-C2-1-R.

References

[1] J. Conti, P. Holtberg, J. Diefenderfer, A. LaRose, J. T. Turnure, L. Westfall, International energy outlook 2016 with projections to 2040, Tech. rep. (2016). doi:https://doi.org/10.2172/1296780.

[2] S. Solaymani, Co2 emissions patterns in 7 top carbon emitter economies: the case of transport sector, Energy 168 (2019) 989–1001.

[3] A. La Notte, S. Tonin, G. Lucaroni, Assessing direct and indirect emissions of greenhouse gases in road transportation, taking into account the role of uncertainty in the emissions inventory, Environmental Impact Assessment Review 69 (2018) 82–93. doi:https://doi.org/10.1016/j.eiar.2017.11.008.

[4] C. Böhringer, The kyoto protocol: a review and perspectives, Oxford Review of Economic Policy 19 (3) (2003) 451–466.

[5] N. Höhne, T. Kuramochi, C. Warnecke, F. Röser, H. Fekete, M. Hagemann, T. Day, R. Tewari, M. Kurdziel, S. Sterl, et al., The paris agreement: resolving the inconsistency between global goals and national contributions, Climate Policy 17 (1) (2017) 16–32. doi:https://doi.org/10.1080/14693062.2016.1218320.

[6] B. Ashok, A. N. Kumar, A. Jacob, R. Vignesh, Emission formation in ic engines, in: NOx Emission Control Technologies in Stationary and Automotive Internal Combustion Engines, 2022, pp. 1–38. doi:https://doi.org/10.1016/B978-0-12-823955-1.00001-2.

[7] A. Vressner, P. Gabrielsson, I. Gekas, E. Senar-Serra, Meeting the euro vi nox emission legislation using a euro iv base engine and a scr/asc/doc/dpf configuration in the world harmonized transient cycle, Tech. rep. (2010). doi:https://doi.org/10.4271/2010-01-1216.

[8] J. R. Serrano, R. Novella, J. Gomez-Soriano, P. J. Martinez-Hernandiz, Computational methodology for knocking combustion analysis in compression-ignited advanced concepts, Applied Sciences 8 (10) (2018) 1707. doi:10.3390/app8101707.

[9] S. Cho, C. Song, N. Kim, S. Oh, D. Han, K. Min, Influence of the wall temperatures of the combustion chamber and intake ports on the charge temperature and knock characteristics in a spark-ignited engine, Applied Thermal Engineering 182 (2021) 116000. doi:https://doi.org/10.1016/j.applthermaleng.2020.116000.

[10] R. M. Heck, R. J. Farrauto, Automobile exhaust catalysts, Applied Catalysis A: General 221 (1-2) (2001) 443–457. doi:https://doi.org/10.1016/S0926-860X(01)00818-3.

[11] S. Biswas, L. Qiao, Ignition of ultra-lean premixed hydrogen/air by an impinging hot jet, Applied energy 228 (2018) 954–964. doi:https://doi.org/10.1016/j.apenergy.2018.06.102.

[12] J. M. Desantes, J. J. López, R. Novella, J. Antolini, Pre-chamber ignition systems: A methodological proposal to reproduce a reference case in a simplified experimental facility for fundamental studies, International Journal of Engine Research 22 (11) (2021) 3358–3371. doi:https://doi.org/10.1177/1468087420971115.

[13] C. E. C. Alvarez, G. E. Couto, V. R. Roso, A. B. Thiriet, R. M. Valle, A review of prechamber ignition systems as lean combustion technology for si engines, Applied Thermal Engineering 128 (2018) 107–120. doi:https://doi.org/10.1016/j.applthermaleng.2017.08.118.

[14] E. Toulson, H. J. Schock, W. P. Attard, A review of pre-chamber initiated jet ignition combustion systems, Tech. rep. (2010). doi:https://doi.org/10.4271/2010-01-2263.

[15] W. P. Attard, P. Parsons, A normally aspirated spark initiated combustion system capable of high load, high efficiency and near zero nox emissions in a modern vehicle powertrain, SAE International Journal of Engines 3 (2) (2010) 269–287.

[16] W. P. Attard, H. Blaxill, A lean burn gasoline fueled pre-chamber jet ignition combustion system achieving high efficiency and low nox at part load, Tech. rep. (2012). doi:https://doi.org/10.4271/2012-01-1146.

[17] S. Zhu, S. Akehurst, A. Lewis, H. Yuan, A review of the pre-chamber ignition system applied on future low-carbon spark ignition engines, Renewable and Sustainable Energy Reviews 154 (2022) 111872. doi:https://doi.org/10.1016/j.rser.2021.111872.

[18] S. Heyne, M. Meier, B. Imbert, D. Favrat, Experimental investigation of prechamber autoignition in a natural gas engine for cogeneration, Fuel 88 (3) (2009) 547 – 552. doi:https://doi.org/10.1016/j.fuel.2008.09.032.
URL http://www.sciencedirect.com/science/article/pii/S0016236108003712

[19] P. Chinnathambi, B. Thelen, D. Cook, E. Toulson, Performance metrics for fueled and unfueled turbulent jet igniters in a rapid compression machine, Applied Thermal Engineering 182 (2021) 115893. doi:https://doi.org/10.1016/j.applthermaleng.2020.115893.

[20] C. Müller, S. Pischinger, S. Tews, A. Müller, K. Habermann, Analysis of experimental results with an active pre-chamber ultra-lean burn si engine, International Journal of Engine Research 22 (10) (2021) 3103–3127. doi:https://doi.org/10.1177/1468087420974544.

[21] S. Biswas, L. Qiao, Ignition of ultra-lean premixed h2/air using multiple hot turbulent jets generated by pre-chamber combustion, Applied Thermal Engineering 132 (2018) 102–114. doi:https://doi.org/10.1016/j.applthermaleng.2017.11.073.

[22] G. Gentz, M. Gholamisheeri, E. Toulson, A study of a turbulent jet ignition system fueled with iso-octane: Pressure trace analysis and combustion visualization, Applied energy 189 (2017) 385–394. doi:https://doi.org/10.1016/j.apenergy.2016.12.055.

[23] F. Li, Z. Zhao, B. Wang, Z. Wang, Experimental study of pre-chamber jet ignition in a rapid compression machine and single-cylinder natural gas engine, International Journal of Engine Research 22 (4) (2021) 1342–1356. doi:https://doi.org/10.1177/1468087419883783.

[24] J. Benajes, R. Novella, J. Gomez-Soriano, P. Martinez-Hernandiz, C. Libert, M. Dabiri, Evaluation of the passive pre-chamber ignition concept for future high compression ratio turbocharged spark-ignition engines, Applied Energy 248 (2019) 576–588. doi:https://doi.org/10.1016/j.apenergy.2019.04.131.

[25] J. López, R. Novella, J. Gomez-Soriano, P. Martinez-Hernandiz, F. Rampanarivo, C. Libert, M. Dabiri, Advantages of the unscavenged prechamber ignition system in turbocharged natural gas engines for automotive applications, Energy 218 (2021) 119466. doi:https://doi.org/10.1016/j.energy.2020.119466.

[26] R. Novella, J. Gomez-Soriano, P. Martinez-Hernandiz, C. Libert, F. Rampanarivo, Improving the performance of the passive prechamber ignition concept for spark-ignition engines fueled with natural gas, Fuel 290 (2021) 119971. doi:https://doi.org/10.1016/j.fuel.2020.119971.

[27] M. Sens, E. Binder, P. Reinicke, M. Riess, et al., Pre-chamber ignition and promising complementary technologies, in: 27th Aachen Colloquium, Aachen, 2018.

[28] C. Hu, Z. Zhang, M. Tian, N. Liu, S. Wei, Research on application of asymmetrical pre-chamber in air-assisted direct injection kerosene engine, Applied Thermal Engineering 204 (2022) 117919. doi:https://doi.org/10.1016/j.applthermaleng.2021.117919.

[29] S. Posch, H. Winter, J. Zelenka, G. Pirker, A. Wimmer, Development of a tool for the preliminary design of large engine prechambers using machine learning approaches, Applied Thermal Engineering 191 (2021) 116774. doi:https://doi.org/10.1016/j.applthermaleng.2021.116774.

[30] J. Benajes, R. Novella, J. Gomez-Soriano, I. Barbery, C. Libert, F. Rampanarivo, M. Dabiri, Computational assessment towards understanding the energy conversion and combustion process of lean mixtures in passive pre-chamber ignited engines, Applied Thermal Engineering 178 (2020) 115501. doi:https://doi.org/10.1016/j.applthermaleng.2020.115501.

[31] J. Benajes, R. Novella, J. Gomez-Soriano, I. Barbery, C. Libert, Advantages of hydrogen addition in a passive pre-chamber ignited si engine for passenger car applications, International Journal of Energy Research 45 (9) (2021) 13219–13237. doi:https://doi.org/10.1002/er.6648.

[32] J. Benajes, R. Novella, J. Gomez-Soriano, P. Martinez-Hernandiz, C. Libert, M. Dabiri, Performance of the passive pre-chamber ignition concept in a spark-ignition engine for passenger car applications, in: SIA Power Train & Electronics, SIA Power Train & Electronics, Paris, France, 2019.

[33] F. Payri, S. Molina, J. Martín, O. Armas, Influence of measurement errors and estimated parameters on combustion diagnosis, Applied Thermal Engineering 26 (2) (2006) 226 – 236. doi:https://doi.org/10.1016/j.applthermaleng.2005.05.006.
URL http://www.sciencedirect.com/science/article/pii/S1359431105001560

[34] C. Guardiola, J. López, J. Martín, D. García-Sarmiento, Semiempirical in-cylinder pressure based model for nox prediction oriented to control applications, Applied Thermal Engineering 31 (16) (2011) 3275–3286. doi:https://doi.org/10.1016/j.applthermaleng.2011.05.048.

[35] M. Lapuerta, O. Armas, J. Hernández, Diagnosis of di diesel combustion from in-cylinder pressure signal by estimation of mean thermodynamic properties of the gas, Applied Thermal Engineering 19 (5) (1999) 513 – 529. doi:https://doi.org/10.1016/S1359-4311(98)00075-1.
URL http://www.sciencedirect.com/science/article/pii/S1359431198000751

[36] J. Benajes, P. Olmeda, J. Martín, R. Carreño, A new methodology for uncertainties characterization in combustion diagnosis and thermodynamic modelling, Applied Thermal Engineering 71 (1) (2014) 389–399. doi:https://doi.org/10.1016/j.applthermaleng.2014.07.010.

[37] CONVERGENT SCIENCE Inc., CONVERGE 2.4 Theory Manual (2018).

[38] R. Novella, J. Pastor, J. Gomez-Soriano, I. Barbery, C. Libert, F. Rampanarivo, C. Panagiotis, M. Dabiri, Experimental and numerical analysis of passive pre-chamber ignition with egr and air dilution for future generation passenger car engines, Tech. rep. (2020). doi:https://doi.org/10.4271/2020-01-0238.

[39] V. Yakhot, S. A. Orszag, Renormalization group analysis of turbulence. i. basic theory, Journal of scientific computing 1 (1) (1986) 3–51. doi:https://doi.org/10.1007/BF01061452.

[40] R. Cant, Sb pope, turbulent flows, cambridge university press, cambridge, uk, Combustion and Flame 125 (2001) 1361–1362. doi:http://dx.doi.org/10.1016/S0010-2180(01)00244-9.
[41] F. E. Marble, J. E. Broadwell, The coherent flame model for turbulent chemical reactions, Tech. rep., PURDUE UNIV LAFAYETTE IN PROJECT SQUIDHEADQUARTERS (1977).
[42] P. Boudier, S. Henriot, T. Poinsot, T. Baritaud, A model for turbulent flame ignition and propagation in spark ignition engines, in: Symposium (International) on Combustion, Vol. 24, 1992, pp. 503–510. doi:https://doi.org/10.1016/S0082-0784(06)80064-0.
[43] O. Colin, A. Benkenida, C. Angelberger, 3d modeling of mixing, ignition and combustion phenomena in highly stratified gasoline engines, Oil & gas science and technology 58 (1) (2003) 47–62. doi:https://doi.org/10.2516/ogst:2003004.
[44] O. Colin, A. Benkenida, The 3-zones extended coherent flame model (ecfm3z) for computing premixed/diffusion combustion, Oil & Gas Science and Technology 59 (6) (2004) 593–609. doi:https://doi.org/10.2516/ogst:2004043.
[45] T. Poinsot, D. Veynante, Theoretical and numerical combustion, RT Edwards, Inc., 2005.
[46] O. Colin, K. Truffin, A spark ignition model for large eddy simulation based on an fsd transport equation (issim-les), Proceedings of the Combustion Institute 33 (2) (2011) 3097–3104. doi:https://doi.org/10.1016/j.proci.2010.07.023.
[47] J. Duclos, O. Colin, (2-25) arc and kernel tracking ignition model for 3d spark-ignition engine calculations ((si-7) si engine combustion 7-modeling), in: The Proceedings of the International symposium on diagnostics and modeling of combustion in internal combustion engines 01.204, 2001, p. 46. doi:https://doi.org/10.1299/jmsesdm.01.204.46.
[48] Y.-D. Liu, M. Jia, M.-Z. Xie, B. Pang, Enhancement on a skeletal kinetic model for primary reference fuel oxidation by using a semidecoupling methodology, Energy & Fuels 26 (12) (2012) 7069–7083. doi:https://doi.org/10.1021/ef301242b.
[49] H. Wang, M. Yao, R. D. Reitz, Development of a reduced primary reference fuel mechanism for internal combustion engine combustion simulations, Energy & Fuels 27 (12) (2013) 7843–7853. doi:https://doi.org/10.1021/ef401992e.
[50] L. Cai, H. Pitsch, Optimized chemical mechanism for combustion of gasoline surrogate fuels, Combustion and flame 162 (5) (2015) 1623–1637. doi:https://doi.org/10.1016/j.combustflame.2014.11.018.
[51] M. Mehl, W. J. Pitz, C. K. Westbrook, H. J. Curran, Kinetic modeling of gasoline surrogate components and mixtures under engine conditions, Proceedings of the Combustion Institute 33 (1) (2011) 193–200. doi:https://doi.org/10.1016/j.proci.2010.05.027.
[52] J. Brakora, R. D. Reitz, A comprehensive combustion model for biodiesel-fueled engine simulations, Tech. rep. (2013). doi:https://doi.org/10.4271/2013-01-1099.
[53] K. Fieweger, R. Blumenthal, G. Adomeit, Self-ignition of si engine model fuels: a shock tube investigation at high pressure, Combustion and Flame 109 (4) (1997) 599–619. doi:https://doi.org/10.1016/S0010-2180(97)00049-7.
[54] S. Jerzembeck, N. Peters, P. Pepiot-Desjardins, H. Pitsch, Laminar burning velocities at high pressure for primary reference fuels and gasoline: Experimental and numerical investigation, Combustion and Flame 156 (2) (2009) 292–301. doi:https://doi.org/10.1016/j.combustflame.2008.11.009.
[55] A. Torregrosa, P. Olmeda, B. Degraeuwe, M. Reyes, A concise wall temperature model for di diesel engines, Applied Thermal Engineering 26 (11-12) (2006) 1320–1327. doi:https://doi.org/10.1016/j.applthermaleng.2005.10.021.
[56] G. Xu, Y. M. Wright, M. Schiliro, K. Boulouchos, Characterization of combustion in a gas engine ignited using a small un-scavenged pre-chamber, International Journal of Engine Research (2018) 1468087418798918doi:https://doi.org/10.1177/1468087418798918.
[57] P. Chinnathambi, M. Bunce, L. Cruff, Rans based multidimensional modeling of an ultra-lean burn pre-chamber combustion system with auxiliary liquid gasoline injection, Tech. rep. (2015). doi:10.4271/2015-01-0386.
[58] K. Bardis, G. Xu, P. Kyrtatos, Y. M. Wright, K. Boulouchos, A zero dimensional turbulence and heat transfer phenomenological model for pre-chamber gas engines, Tech. rep. (2018). doi:https://doi.org/10.4271/2018-01-1453.
[59] C. Angelberger, T. Poinsot, B. Delhay, Improving near-wall combustion and wall heat transfer modeling in si engine computations, Tech. rep. (1997). doi:https://doi.org/10.4271/972881.

List of symbols/abbreviations

SI: Spark ignition
CI: Compression ignition
TJI: Turbulent jet ignition
MC: Main combustion chamber
PC: Pre-chamber
ICE: Internal combustion engine
CFD: Computational fluid dynamics
NO_x: Nitrogen oxides
TWC: Three-Way catalyst
PFI: Port fuel injection
$DOHC$: Double over-head camshaft
CO_2: Carbon dioxide
λ: Relative air-to-fuel ratio
$RON95$: 95 Research Octane Number
CCV: cycle-to-cycle variability
TDC: Top dead center
BDC: Bottom dead center
ST: Spark timing
CAD: Crank-angle degree
$CADaTDC$: Crank-angle after the Top dead center
$CADaST$: Crank-angle after the Spark timing
HRR: Heat release rate
HR: Heat release
Δp: Pressure difference between the pre-chamber and main chamber
$IMEP$: Indicated mean effective pressure
$\sigma IMEP$: Variability of the IMEP
MBT: Maximum break torque
$URANS$: Unsteady Reynolds-averaged Navier Stokes
$ECFM$: Extended Coherent Flamelet Model
TKE: Turbulent kinetic energy
RGF: Residual Gas Fraction
EAE: Energy available for ejection
Q_{wall}: Heat losses through the pre-chamber walls
$Unburnt$: fuel mass left in the pre-chamber after the ejection has ended
$Inert$: Non-reacting mass ejected from the pre-chamber

List of Figures

List of Tables